An agent-based modeling approach for lung fibrosis in response to COVID-19

Mohammad Aminul Islam[1], Michael Getz[2], Paul Macklin[2], Ashlee N. Ford Versypt[1*]

1 Department of Chemical and Biological Engineering, University at Buffalo, The State University of New York, Buffalo, NY, 14260, USA
2 Department of Intelligent Systems Engineering, Indiana University, Bloomington, IN, 47408, USA

* ashleefv@buffalo.edu

Abstract

The severity of the COVID-19 pandemic has created an emerging need to investigate the long-term effects of infection on patients. Many individuals are at risk of suffering pulmonary fibrosis due to the pathogenesis of lung injury and impairment in the healing mechanism. Fibroblasts are the central mediators of extracellular matrix deposition during tissue regeneration, regulated by anti-inflammatory cytokines including TGF-β. The TGF-β-dependent accumulation of fibroblasts at the damaged site and excess fibrillar collagen deposition lead to fibrosis. We developed an open-source, multiscale tissue simulator to investigate the role of TGF-β sources in the progression of lung fibrosis after SARS-COV-2 exposure, intracellular viral replication, infection of epithelial cells, and host immune response. Using the model, we predicted the dynamics of fibroblasts, TGF-β, and collagen deposition for 15 days post-infection in virtual lung tissue. Our results showed variation in collagen area fractions between 2% and 40% depending on the spatial behavior of the sources (stationary or mobile), the production rate of TGF-β, and the activation duration of TGF-β sources. We identified M2 macrophages as primary contributors to higher collagen area fraction. Our simulation results also predicted fibrotic outcomes even with lower collagen area fraction for a longer activation duration of latent TGF-β sources. Our results showed changes in fibrotic patterns with partial removal of TGF-β sources and significantly increased collagen area fraction with partial removal of TGF-β from the extracellular matrix in the presence of persistent latent TGF-β sources. These critical insights into the activity of TGF-β sources may find applications in the current clinical trials targeting TGF-β for the resolution of lung fibrosis.

Author summary

COVID-19 survivors are at risk of lung fibrosis as a long-term effect. Lung fibrosis is the excess deposition of tissue materials in the lung that hinder gas exchange and can collapse the whole organ. We identified TGF-β as a critical regulated of fibrosis. We built a model to investigate the mechanisms of TGF-β sources in the process of fibrosis. Our results showed spatial behavior of sources (stationary or mobile) and their activity (production rate of TGF-β, longer activation of sources) could lead to lung fibrosis. Current clinical trials for fibrosis that target TGF-β need to consider TGF-β sources' spatial properties and activity to develop better treatment strategies.

Introduction

Severe acute respiratory syndrome coronavirus 2 (SARS-CoV-2) is responsible for the coronavirus disease 19 (COVID-19) pandemic and primarily causes pulmonary infection resulting in short-term pneumonia to long-term acute respiratory distress syndrome (ARDS), among other symptoms and complications [1–3]. The long-term respiratory complications of COVID-19 survivors include diffuse alveolar damage (DAD), which is also a histological hallmark of ARDS [4]. DAD begins with the exudative phase when edema and inflammation occur, followed by the fibroproliferative phase with loose organizing fibrosis. In the fibroproliferative phase, damaged tissues are partially replaced through fibroblast migration, proliferation, and collagen deposition. But impairments in the repair mechanisms—such as persistent infections [5], imbalance between profibrotic and antifibrotic mediators [6], and dysregulation in the functions of immune cells [7, 8] and fibroblasts [9, 10]—can lead to long-term fibrosis.

The severity of SARS-CoV-2 infection dictates the severity of pulmonary fibrosis. Zou et al. [11] reported that 100% of patients with severe and critical COVID-19 disease generate pulmonary fibrosis, wherein severe fibrosis is observed in most cases. Although 90-day follow-up results in their experiments showed significant resolution in most patients, some patients had fibrotic areas after 90 days. In another study, Li et al. [2] reported that 59.6% of patients with confirmed COVID-19 cases had lung fibrosis after 90 days from onset. The overall lung fibrosis in hospitalized patients was 86.87%, out of which only 31.74% of patients had eventual resolution of fibrosis in follow-up visits. The six-month follow-up computed tomography scan of severe COVID-19 pneumonia survivors in the study of Han et al. [12] showed fibrotic changes in 35% of patients. They identified that susceptible groups have ARDS, higher heart rate, older age, longer hospital stay, and noninvasive mechanical ventilation. COVID-19 pulmonary fibrosis is different from other fibrotic lung diseases, e.g., idiopathic pulmonary fibrosis (IPF), as injuries occur at the site of epithelial cells rather than endothelial cells [3]. Currently, mechanistic basics for progressive and stable fibrosis resolution are not completely understood.

Macrophages play an essential role in different phases of DAD. Inflammatory macrophages (M1 macrophages) are activated during the exudative phase of tissue damage to provide host defense [13]. At the same time, M1 macrophages are responsible for inflammation and lung injury. In the fibroproliferative phase of DAD, M1 macrophages shift to alternatively activated macrophages (M2 macrophages) and start secreting anti-inflammatory cytokines (e.g., TGF-β), clearing apoptotic cells, and removing debris [14]. M2 macrophages play a crucial role in developing and resolving tissue damage in the fibroproliferative and fibrotic stages of DAD [15, 16].

Another critical contributor to fibrosis is the activation of latent TGF-β due to tissue damage. Latent TGF-β is stored at high concentrations in the extracellular matrix (ECM) in an inactive state in most organs, including the lung [17]. Injury or death of epithelial cells due to external stimuli activate the latent TGF-β at the damaged sites using $\alpha\nu\beta 6$ integrins [9, 18]. Latent TGF-β can also be activated by reactive oxygen species (ROS), low pH, and proteolysis [19].

Other sources of TGF-β in pulmonary fibrosis are metaplastic type II alveolar epithelial cells (AECs), bronchial epithelium, eosinophils, fibroblasts, and myofibroblasts [19, 20]. Depending on the spatial behavior of sources, they can be categorized into two groups: stationary sources (e.g., latent TGF-β) and mobile sources (e.g., M2 macrophages). Overexpression of TGF-β from any source and the persistent presence of any source can lead to fibrosis. Experimental observations in rat models showed the progression of pulmonary fibrosis with overexpression of TGF-β [21]. Also, quantification of TGF-β in the plasma of COVID-19 patients showed an increase in TGF-β concentration compared to healthy individuals [22, 23].

Activated TGF-β directs the functions of fibroblasts. Resident fibroblasts are located beneath epithelial cells or scattered in the ECM between the lung's epithelial and endothelial layers [24]. The accumulation of TGF-β due to viral infection and epithelial cell injury recruit fibroblasts [25]. Small injuries can be repaired by proliferation and differentiation of type 2 AECs to type 1 AECs. In contrast, the restoration process fails in severe injuries, leading to fibroblast activation and fibrosis [9]. Activated fibroblasts continually secrete ECM (e.g., collagen) to maintain the structural integrity of the lung [26]. TGF-β also regulates the collagen deposition rate of fibroblasts. The experimental studies of Good et al. [27] reported TGF-β dependency of fibroblasts in collagen deposition in the case of IPF.

The current identification methods of lung fibrosis include histologic analysis of tissue samples and radiographic examination with computed tomography [28, 29]. Fibrotic pattern, collagen area fraction, and localization of cells can be observed from the histological analysis. Collagen area fractions evaluated from histopathological images are strongly correlated with histologic fibrosis scores and provide a reliable index to quantify fibrosis [30].

Existing mathematical and computational models can give insights into the fundamental processes that regulate fibrotic outcomes. Brown et al. [31] developed a simple agent-based model (ABM) considering the effects of the pro-inflammatory mediator TNF-α in tissue damage and the anti-inflammatory mediator TGF-β1 in fibroblast-mediated collagen deposition due to exposure to smoke particles. Their model captured the histological observation of self-resolving tissue damage, localized tissue damage with fibrosis, and extensive tissue damage with fibrotic states. The ABM of Warsinske et al. [32] explored the co-regulatory relationship between epithelial cells and fibroblasts through TGF-β1 during fibrosis. In another 3D ABM of lung fibrosis [33], the initial amount of damaged type 2 AECs activated the inactive TGF-β. The ABM of Ceresa et al. [34] focused on emphysema progression (excess degradation of collagen) in chronic obstructive pulmonary disease and considered the transition of macrophages between the M1 and M2 phenotypes, secretion of TGF-β from M2 macrophages, recruitment of fibroblasts by TGF-β, fibroblast-mediated collagen deposition, and collagen degradation by MMP9. The mathematical model of Hao et al. [35] used continuous partial differential equations for IPF and considered crucial cells and cytokines for the fibrosis process, including the transition of M1 macrophages to M2 phenotype and TGF-β-mediated fibroblast proliferation. Their results showed how treatments that block the activity of cytokines (e.g., anti-TGF-β) could reduce excess formation of ECM. Another relevant study combined experiments and mathematical modeling to investigate the role of TGF-β in fibroblast-mediated collagen deposition during myocardial infarction (MI) [36]. Chowkwale et al. [37] also investigated the inflammation-fibrosis coupling during MI considering the activation of latent TGF-β and TGF-β-dependent fibroblasts proliferation. The coupled ABM and logic-based model of Rikard et al. [38] simulated similar increases in collagen area fractions to experimental observations during MI. Their model also considered the generation of latent TGF-β and fibroblast-mediated collagen deposition. In summary, TGF-β and fibroblasts are standard players in fibrosis progression in all the models described above, and major sources of TGF-β are M2 macrophages and latent TGF-β. Although none of the models considered fibrosis due to viral infection, the process of fibrosis due to SARS-CoV-2 infection involves similar cells and mediators.

We developed a multiscale tissue simulator that can be used to investigate the mechanisms of intracellular viral replication, infection of epithelial cells, host immune response, and tissue damage [39]. Here, we focused on the mechanisms of the fibrotic process in the lung tissue during SARS-CoV-2 infection. We conducted *in silico* experiments to determine the effects of the spatial behavior of TGF-β sources

(stationary and mobile), the production rate of TGF-β from sources, and the activation duration of TGF-β sources in the development and progression of fibrosis. We used collagen area fractions from histological analysis to compare the outcomes of our model simulations.

Methods

Overall model

In our earlier work, we developed a SARS-CoV-2 tissue simulator [39], which we refer to as the "overall model". Here, we briefly recap the most salient features of this overall model before describing our new contribution: the fibrosis model. The overall model structure is developed in an open-source multiscale ABM framework PhysiCell [40] and simulates a tissue section of 800 μm × 800 μm × 20 μm, representing a monolayer of stationary epithelial cells on an alveolar surface of lung tissue. Initially, 2793 epithelial cells, 50 resident macrophages, 28 dendritic cells, and 57 fibroblasts are present in the simulated tissue. These initializations were taken directly from [39]; here we hold maintain the same cellular initializations, with the exception of allowing the initial number of fibroblasts to vary. Cells are recruited to tissue through voxels that represent vasculature points; we randomly assign 8.8% voxels as vasculature points for arrivals of recruited cells because approximately this percentage of the tissue consists of the vasculature [41]. Cellular movement and diffusion of substrates occur along a 2D plane through or above the tissue, represented by a single layer of 3D voxels; this is consistent with the transport through thin alveolar tissue. We infect the simulated tissue by placing SARS-CoV-2 viral particles in the extracellular space using a uniform random distribution. Viral particles diffuse through tissue, bind with unoccupied ACE2 receptors on the epithelial cell surfaces, internalize via endocytosis, replicate through intracellular viral replication kinetics, and export back to the extracellular domain by exocytosis. Details of the intracellular virus model for replication kinetics, viral response, and receptor trafficking are described in much greater detail in our earlier manuscript [39]. After the infection, innate and adaptive immune cells become activated. In the early phase of infection, macrophages, neutrophils, and dendritic cells are recruited as innate immune cells and are subsequently activated in the presence of viral particles and infected cells. We consider five states of macrophages: inactivated, M1 phenotype, M2 phenotype, hyperactive, and exhausted. Both M1 and M2 phenotypes can also exist in hyperactive and exhausted states. Infected cells and M1 macrophages secrete pro-inflammatory cytokines that recruit other immune cells. Macrophages and neutrophils move along the gradient of debris from dead cells, phagocytose dead cells, and clear viral particles. Dendritic cells emigrate to the lymph node and recruit CD4+ T cells and CD8+ T cells. CD8+ T cells kill infected cells. Immune cells move along the gradient of chemokine secreted from infected cells. Further details of the immune and lymph node models are available elsewhere [39, 42]. The repository for version 5.0 of the overall model is available at github.com/pc4covid19/pc4covid19/releases/tag/v5.0 [43].

Fibrosis model

We extended the overall model to include the mechanisms for fibrosis (Fig 1). We used the ABM platform PhysiCell to simulate the rules for phenotypic and mechanical changes, including cell cycle, volume changes, death processes, cellular movement, and recruitment of the agents in Fig 1, in addition to the other processes included in the overall model. We have provided our code in a repository at github.com/ashleefv/covid19fibrosis [44].

Specifically in the fibrosis model, the death of an infected epithelial cell (I) activates the latent TGF-β embedded in the tissue. The activation of latent TGF-β is represented by creating a stationary secreting agent (S) at the site and time of epithelial cell death. The secreting agents secrete TGF-β for a certain period as the amount of TGF-β stored in the ECM is limited; a death rate of secreting agents (AT) is used to represent the termination of the activation of latent TGF-β. Macrophages are the mobile sources of TGF-β in this model. M1 macrophages are recruited in the initial phase, and CD8+ T cells are recruited in the later stage of infection. Usually, regulatory T cells (Tregs), a subset of CD4+ T cells, are involved in the phenotypic transformation of M1 to M2 macrophages [14]. Although we do not have Tregs in the current model, CD8+ T cells exhibit similar behavior by inhibiting the secretion of pro-inflammatory cytokines from M1 macrophages in the later phase of infection [39]. Since the fibroproliferative phase of DAD occurs in the later phase of the disease, a condition is included in the model to follow this pathology: if a CD8+ T cell and an M1 macrophage are within close proximity, then the M1 macrophage stops secreting pro-inflammatory cytokine, transforms to an M2 macrophage, and starts secreting TGF-β. The interaction distance for this transition is calculated using a multiple (ϵ) of the radii of the two interacting immune cells [39]. We simulated the transformation of M1 to M2 phenotype to occur instantaneously when the distance between an M1 macrophage and a CD8+ T cell is $\leq \epsilon$ multiplied by the sum of the radii of the M1 macrophage and the CD8+ T cell). TGF-β activates the resident inactive fibroblasts and recruits new active fibroblasts. The activated fibroblasts chemotax along the gradient of TGF-β and deposit collagen continuously. The newly deposited collagen is assumed to not diffuse or degrade.

Eq 1 describes TGF-β-dependent recruitment rate of fibroblasts $F_g(T_\beta)$ [34, 36]. We selected a threshold value of TGF-β concentration because of the polynomial nature of the recruitment signal (Supplementary File: Fig S1A).

$$F_g(T_\beta) = \begin{cases} 0.0492T_\beta^3 - 0.9868T_\beta^2 + 6.5408T_\beta + 7.1092, & \text{if } 0 < T_\beta \leq 10 \\ 22.928, & \text{else if } T_\beta > 10 \\ 0, & \text{otherwise} \end{cases} \tag{1}$$

The number of recruited fibroblasts to the tissue is determined by integrating the recruitment signal over the whole domain:

$$\text{\# of recruited cells} = r_{recruit} \int_\Omega \min(1, \max(0, \frac{\rho_{cytokine} - \rho_{min}}{\rho_{sat} - \rho_{min}}))dV\Delta t_r \tag{2}$$

where Ω is the computational domain, $r_{recruit}$ is the recruitment rate (per volume), ρ_{min} is the minimum recruitment signal, ρ_{sat} is the saturating or maximum signal, and $\rho_{cytokine}$ is the recruitment rate of a cytokine. We consider the volume of each grid as $dV = 20 \times 20 \times 20\ \mu\text{m}^3$ and the time interval for recruitment of fibroblasts as $\Delta t_r = 10$ min, the same as the overall model [39]. Eq 2 is general for recruitment of any immune cell by a specific cytokine in the overall model; CD8+ T cells and macrophages are already included in the overall model [39]. Here we take $\rho_{cytokine} = F_g(T_\beta)$ for the recruitment rate of fibroblasts via the cytokine TGF-β.

PhysiCell is coupled to BioFVM [45], which solves partial differential equations of diffusion, decay, uptake, and release of multiple substances simultaneously. We simulate extracellular concentrations of TGF-β (T_β) using the standard BioFVM formulation:

$$\frac{\partial T_\beta}{\partial t} = D_{T\beta}\nabla^2 T_\beta - \mu_{T\beta}T_\beta + \sum_{cells\ i} \delta(x - x_i)E_{T\beta,i} \tag{3}$$

where t is time, $D_{T\beta}$ is the diffusion coefficient of TGF-β, $\mu_{T\beta}$ is the net decay rate, $\delta(x)$ is the discrete Dirac delta function, x is the position of the voxel, x_i is the position

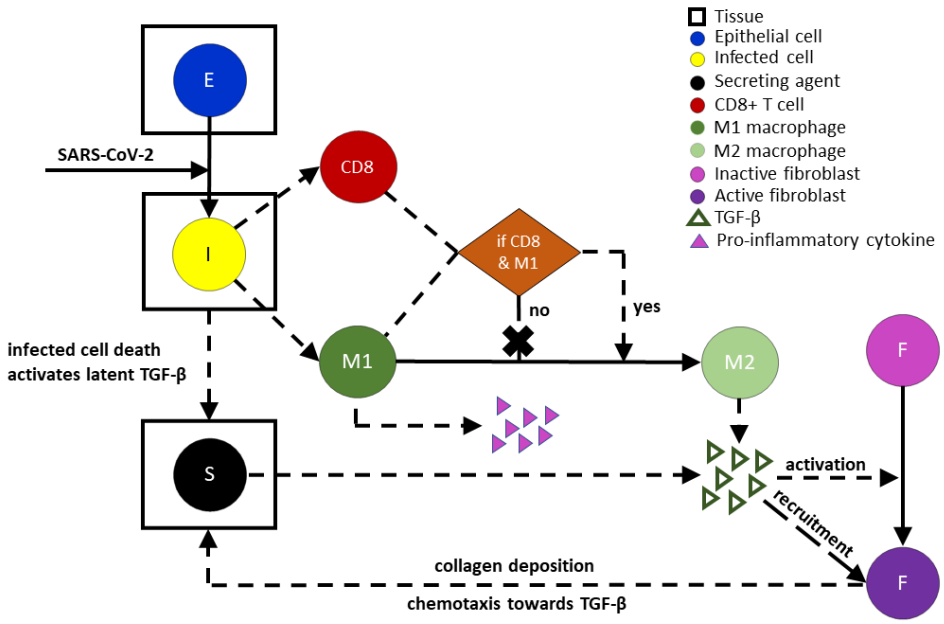

Fig 1. Cellular and extracellular mediators in lung fibrosis during SARS-CoV-2 infection included in the fibrosis model. Secreting agents (S) mimic the activation of latent TGF-β by acting as stationary sources of TGF-β for a certain period at the site and time of dead infected epithelial cells (I). I recruit M1 macrophages initially as innate immune response and CD8+ T cells in the later phase of infection as adaptive immune response. M1 macrophages stop secreting pro-inflammatory cytokines when located within close proximity to CD8+ T cells and instantaneously convert to M2 macrophages. M2 macrophages secrete TGF-β and are considered mobile sources. Fibroblasts become activated and recruited by TGF-β, chemotax towards the gradient of TGF-β, and deposit collagen continuously. Cells with rectangles drawn around them represent stationary cells in tissue sections, while all other cells are considered to be mobile cells. Solid arrows denote the transformation of one cell species to another, the X over an arrow indicates the transformation does not occur, and dotted lines denote interactions that influence processes without the source being produced or consumed. Triangles represent secreted factors that can diffuse and interact in the system.

of the center of cell i, and $E_{T\beta,i}$ is the net export rate of TGF-β from cell i. Net export rate $E_{T\beta,i}$ denotes latent TGF-β activation rate from damaged site, which we term damaged-site secretion (DS), or TGF-β secretion rate from macrophages, which we term macrophage secretion (MS). We assume that inactive fibroblasts become active fibroblasts in the presence of TGF-β ($T_\beta > 0$) and switch back to the inactive state in the absence of TGF-β ($T_\beta = 0$).

TGF-β-dependent collagen deposition from fibroblasts is described in Eqs 4-5 considering a Michaelis-Menten relationship to quantify the TGF-β dependence:

$$\frac{\partial C}{\partial t} = \sum_{cells\ i} \delta(x - x_i) E_{C,i} \tag{4}$$

$$E_{C,i} = k_{FC} F_c(T_\beta) = k_{FC} \frac{V_{T\beta} T_\beta}{k_{T\beta} + T_\beta} \tag{5}$$

where C in the concentration of collagen, $E_{C,i}$ is the net export rate of collagen of cell i, k_{FC} is the collagen production rate by fibroblasts, $F_c(T_\beta)$ is the TGF-β dependence of fibroblast-mediated collagen deposition. $V_{T\beta}$ and $k_{T\beta}$ are the Michaelis-Menten rate and saturation parameters defining the TGF-β dependency on collagen deposition.

Parameter estimation

Experimental data from the literature used in this section are extracted from graphs in the original sources, which are referenced in the text, using the open-source Java program Plot Digitizer [46].

The initial values of the species in the uninfected condition are listed in Table 1. The estimated and calculated parameters are listed in Table 2.

Table 1. Initial conditions for model variables

Symbol	Definition	Initial condition
F	Initial number of fibroblasts	57 cells [47]
C	Initial concentration of collagen	0 μg μm^{-3}
T_β	Initial concentration of TGF-β	0 ng mL^{-1}

Table 2. Parameters for the fibrosis model

Symbol	Definition	Value	Unit	Source
DS	TGF-β activation rate from a damaged site	$5 \times 10^{-10} - 2 \times 10^{-9}$	ng min^{-1}	estimated
MS	TGF-β secretion rate from an M2 macrophage	$5 \times 10^{-10} - 2 \times 10^{-9}$	ng min^{-1}	estimated
$D_{T\beta}$	TGF-β diffusion coefficient	3000	μm^2 min^{-1}	[35]
$\mu_{T\beta}$	TGF-β degradation rate	15	day^{-1}	[34]
k_{FC}	Fibroblast collagen production rate	2.52×10^{-7}	μg min^{-1}	estimated from Ref [35]
V_F	Fibroblast velocity	1	μm min^{-1}	[48]
F_V	Fibroblast cell volume	2500	μm^3	[49]
F_{VN}	Fibroblast nucleus volume	500	μm^3	[50]
μ_F	Fibroblast apoptosis rate	8.30×10^{-5}	min^{-1}	[34]
ρ_{sat}	Maximum/saturating fibroblast recruitment signal of TGF-β	22.928	ng mL^{-1}	calculated by Eq 1
ρ_{min}	Minimum fibroblast recruitment signal of TGF-β	7.1092	ng mL^{-1}	calculated by Eq 1
$r_{recruit}$	Fibroblast recruitment rate	4×10^{-9}	cells μm^{-3} min^{-1}	[39]
AT	Secreting agent death rate	1×10^{-3}	min^{-1}	estimated from [36]
ϵ	Multiple of interaction distance for immune cells	1.75	Unitless	[39]
$V_{T\beta}$	Rate parameter for TGF-β-dependent collagen deposition	9.42×10^{-1}	Unitless	estimated from Ref [51, 52] data
$k_{T\beta}$	Saturation parameter for TGF-β-dependent collagen deposition	1.74×10^{-1}	Unitless	estimated from Ref [51, 52] data
U_F	Uptake rate of TGF-β by fibroblasts	1×10^{-1}	min^{-1}	estimated

The initial number of fibroblasts is selected based on *in vivo* experiments of mice models of MI [47]. We extracted the fibroblast population per surface area from the experimental control condition [47] and multiplied it by the surface area of the computational domain (800×800 μm^2) to evaluate the initial number of inactive resident fibroblasts in the simulated tissue. We considered the changes of TGF-β (T_β) and collagen deposited (C) from homeostatic values and set them to 0 as initial values.

TGF-β-dependent recruitment rate of fibroblasts $F_g(T_\beta)$ and TGF-β-dependent collagen deposition rate from fibroblasts $F_c(T_\beta)$ are defined for TGF-β ranges of 0-10 ng/mL from experiments [51–53] and mathematical models [34, 36]. We calibrated the fibrosis model by adjusting DS and MS to keep TGF-β concentration within the defined range. We iteratively changed DS while $MS = 0$ (turning off secretion from macrophages) and changed MS while $DS = 0$ (turning off secretion from damaged sites) to estimate the concentration range of TGF-β (Fig S2); our goal was to keep TGF-β concentration within the range of experimental observations (0–10 ng/mL) where TGF-β dependency of fibroblasts is defined. We selected ranges of DS from 5×10^{-10} to 2×10^{-9} ng min^{-1} and MS from 5×10^{-10} to 2×10^{-9} ng min^{-1}.

We evaluated the signal of TGF-β to recruit new fibroblasts ($\rho_{cytokine}$) in Eq 2 using TGF-β-dependent fibroblasts recruitment rate from Eq 1, i.e., $\rho_{cytokine} = F_g(T_\beta)$. The

minimum and maximum (i.e., saturating) recruitment signals are calculated using Eq 1 for the lower (0 ng/mL) and upper (10 ng/mL) range of TGF-β, respectively.

Fibroblast collagen production rate k_{FC} is estimated from Hao et al. [35] (details in the Supplementary File). $F_c(T_\beta)$ is the TGF-β dependence on collagen production rate. We normalized published experimental data [51, 52] and performed curve fitting considering the Michaelis-Menten relationship to estimate the parameters $V_{T\beta}$ and $k_{T\beta}$ for $F_c(T_\beta)$ formulation in Eq 5 (Fig S1B).

Results and Discussion

Spatial behaviors of TGF-β sources affect collagen dynamics

We used the fibrosis model to predict the effects of stationary and mobile sources of TGF-β in fibroblast-mediated collagen deposition in the lung tissue during SARS-CoV-2 infection. The stationary sources caused localized collagen deposition, whereas the distribution of collagen was more dispersed for mobile sources (Fig 2). We also observed two distinct peaks in TGF-β dynamics depending on the sources. Initially, death of infected epithelial cells created secreting agents, which were stationary sources that activated latent TGF-β. The number of these secreting agents fixed at damaged sites had a maximum around 5 days post-infection (dpi). The population reduced after that as removal of the virions from the system occurred around 6 dpi (Fig S3). As a result, we observed the first peak in TGF-β concentration around 5 dpi. The constant rate of production and diffusion of TGF-β from stationary sources created localized fields with higher TGF-β concentrations. Active fibroblasts crowded at the sites of higher concentration of TGF-β and deposited collagen to cause localized distribution. In this model, M2 macrophages must appear after the arrival of CD8+ T cells in the later phase of infection as we have encoded the rule that the interactions between M1 macrophages and CD8+ T cells transform M1 macrophages into the M2 phenotype, which act as mobile sources of TGF-β. We observed the maximum number of macrophages around 9 dpi, which caused the second peak in the TGF-β profile. In the later phase of infection, damages were already present in the tissue when M2 macrophages arrived. M2 macrophages moved along the edge of damaged sites, phagocytosed dead and infected cells, cleared viral particles, and simultaneously secreted TGF-β. The movement of M2 macrophages along the edge of damaged sites caused higher concentrations of TGF-β at those sites. As a result, fibroblasts chemotaxed to those sites and deposited collagen. The deposited collagen was more dispersed with a higher collagen area fraction in these cases with mobile sources of TGF-β secretion.

In the case of the equal production rate of TGF-β from damaged sites and macrophages (case DM), we observed localization of fibroblasts around 2 dpi due to the slow creation of new stationary sources (Fig 2A and S4) before the inflammatory response infiltrated the tissue. Around 5 dpi, the sudden increase of stationary sources and the appearance of mobile sources disrupted that localization. Fibroblasts started to move along the edge of damaged sites as the mobile sources moved along the edge to clear infected and dead cells that were more prominent from 9 dpi to 15 dpi. Fibroblasts had partial localization between 5 dpi and 9 dpi. But the locations of localization changed with the disappearance of stationary sources and the appearance of mobile sources. Like case DM, the slow creation of new stationary sources resulted in fibroblasts localization at damaged sites around 2 dpi when the TGF-β secretion rate from macrophages was turned off (case D, Fig S5). The rapid creation of new sources disrupted the localization of fibroblasts around 5 dpi. Localization of fibroblasts was again observed between 5 dpi and 9 dpi followed by delocalization of fibroblasts as stationary sources stopped secreting TGF-β. The absence of TGF-β deactivated

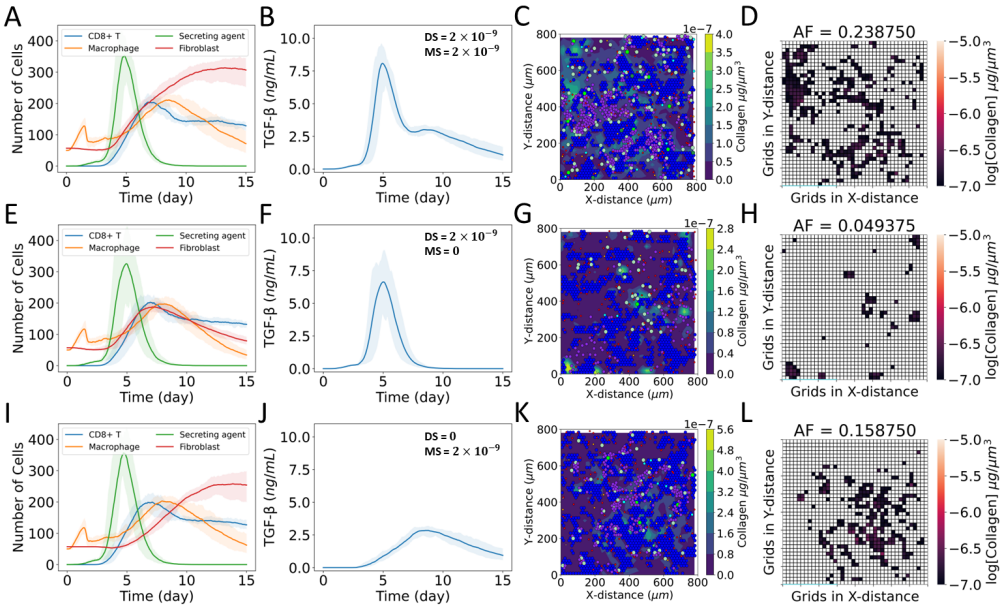

Fig 2. Effects of stationary and mobile sources of TGF-β on the dynamics of collagen deposition. (A–D) TGF-β production from both damaged sites and macrophages (case DM), (E–H) TGF-β activation from damaged sites while secretion rate from macrophages are turned off (case D), (I–L) TGF-β secretion from macrophages while activation rate from damaged sites are turned off (case M). Dynamics of (A, E, I) populations of CD8+ T cells, macrophages, latent TGF-β activation sites (secreting agents), and fibroblasts; (B, F, J) TGF-β concentration spatially averaged over the domain; (C, G, K) collagen deposition at damaged sites of tissue at day 15; (D, H, L) heat map showing collagen area fraction (AF) above threshold value of 1×10^{-7} μg μm^{-3}. The solid curves represent the mean of predictions and shaded areas represent the predictions between the 5th and 95th percentile of 15 replications of the agent-based model. DS = TGF-β activation rate from damaged sites, and MS = TGF-β secretion rate from macrophages. Case DM: equal TGF-β production rate from both stationary damaged sites ($DS = 2 \times 10^{-9}$ ng min^{-1}) and mobile macrophages ($MS = 2 \times 10^{-9}$ ng min^{-1}); case D: TGF-β activation from stationary damaged sites ($DS = 2 \times 10^{-9}$ ng min^{-1}) only, and secretion from mobile macrophages is turned off ($MS = 0$ ng min^{-1}); case M: TGF-β secretion from mobile macrophages only ($MS = 2 \times 10^{-9}$ ng min^{-1}), and activation rate from stationary damaged sites is turned off ($DS = 0$ ng min^{-1}).

fibroblast-mediated collagen deposition after 9 dpi. We did not observe the localization of fibroblasts around 2 dpi in Fig S6, when the TGF-β activation rate from damaged sites was turned off (case M). Around 5 dpi, fibroblasts were observed to move along the edge of damaged areas with the appearance of mobile sources of TGF-β (M2 macrophages), which were more prominent from 9 dpi to 15 dpi. In summary, we observed changes in fibrotic patterns depending on partial creation and deletion of sources, mobility of the sources, and dpi.

The combination of stationary and mobile sources of TGF-β in different phases of infection created higher TGF-β concentration zones at more sites than a single source type, resulting in higher collagen area fractions. The distribution of collagen area fractions is shown in the violin plot in Fig 3. Collagen area fraction was lower in case D,

intermediate in case M, and higher in case DM. In Fig S7, we plotted the dynamics of the spatially averaged collagen concentration for cases DM, D, and M. We observed exponential increases of spatially averaged collagen concentration in cases DM and M with a steeper slope in case DM.

The experiments performed on postmortem transbronchial cryobiopsy samples of COVID-19 pneumonia diseased tissue reported 2%–38% collagen extension considering all the lobes of the lung [28]. In those data, percentage of collagen extensions for different samples were calculated as the ratio between the surface of collagen and the surface of lung tissue. Also, the surface of lung tissue excluded airway walls, vessels, lung structures, and alveolar airspaces, which is similar to our simulation space. Holistically, our simulated collagen area fractions (Fig 3) are in similar ranges (2%–40%) to the experimentally observed percentage of collagen extensions. Our simulated collagen area fractions are also in the similar range to the reported increase of collagen volume fraction in human lung with different stages of IPF [54] and predicted collagen area fractions over time in the multiscale model and experiments of MI [38]. Although the mechanisms for fibrosis may differ in these experiments, our findings suggest that the activity of TGF-β sources is an important aspect, which alone can generate fibrotic areas similar to experimental observations.

Higher TGF-β production rate from M2 macrophages lead to higher collagen area fraction

Next, we explored the effects of the production rate of TGF-β from stationary and mobile sources. In Fig 4, we illustrated the TGF-β dynamics spatially averaged over the domain and the TGF-β impact on the distribution of collagen deposition considering different combinations of production rates from stationary and mobile sources. We observed higher recruitment of fibroblasts for higher production rates of TGF-β from both stationary and mobile sources (case DHMH) and lower activation rate of TGF-β from stationary sources with higher secretion rate of TGF-β from mobile sources (case DLMH). We observed the highest collagen area fraction in case DHMH, followed by case DLMH (Fig 3). In both cases, the TGF-β secretion rate from M2 macrophages was higher. So, mobile sources of TGF-β played a crucial role in higher collagen area fraction, whereas stationary sources were responsible for a more localized distribution of collagen deposition. Lowering the TGF-β production rate of mobile sources (case DHML) or both sources (case DLML) reduced the collagen area fraction significantly. We observed similar population dynamics as case DM in Fig S8–S11 with variations in fibroblast recruitment and collagen area fraction.

Experimental observations of mice models reported that during MI, fibroblasts appeared around day 4, and fibroblasts and collagen deposition remained prominent from day 4 to 21 [47]. We also observed the activation and recruitment of fibroblasts around 4 dpi, and fibroblast population and collagen deposition remained prominent for a higher secretion rate of TGF-β from M2 macrophages (Fig 4A in case DHMH and Fig 4M in case DLMH). The relative abundance of fibroblasts was higher than macrophages in COVID-19 patients [55], which was also observed in the simulation cases we considered. The intercellular model for fibrosis during MI also reported similar dynamics of macrophages, fibroblasts, latent TGF-β, and collagen [37] to some of our simulation cases. However, that model focused on a different organ.

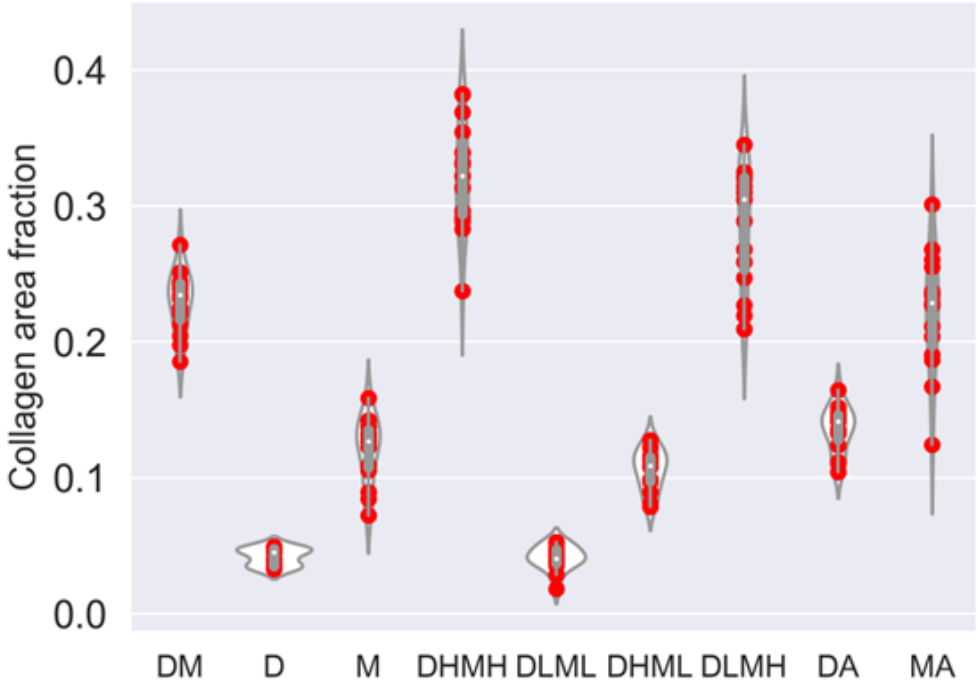

Fig 3. Quantification of collagen area fraction for different cases. Violin plots represent distribution, red solid circles represent data for 15 replications in each of the cases, and box plots shows median and quartiles. Case DM: equal TGF-β production rate from both stationary damaged sites ($DS = 2 \times 10^{-9}$ ng min^{-1}) and mobile macrophages ($MS = 2 \times 10^{-9}$ ng min^{-1}); case D: TGF-β activation from stationary damaged sites ($DS = 2 \times 10^{-9}$ ng min^{-1}) only, and secretion from mobile macrophages is turned off ($MS = 0$ ng min^{-1}); case M: TGF-β secretion from mobile macrophages only ($MS = 2 \times 10^{-9}$ ng min^{-1}), and activation rate from stationary damaged sites is turned off ($DS = 0$ ng min^{-1}); case DHMH: TGF-β activation rate from damaged sites is high ($DS = 2 \times 10^{-9}$ ng min^{-1}), and TGF-β secretion rate from macrophages is high ($MS = 5 \times 10^{-9}$ ng min^{-1}); case DLML: TGF-β activation rate from damaged sites is low ($DS = 5 \times 10^{-10}$ ng min^{-1}), and TGF-β secretion rate from macrophages is low ($MS = 5 \times 10^{-10}$ ng min^{-1}); case DHML: TGF-β activation rate from damaged sites is high ($DS = 2 \times 10^{-9}$ ng min^{-1}), and TGF-β secretion rate from macrophages is low ($MS = 5 \times 10^{-10}$ ng min^{-1}); case DLMH: TGF-β activation rate from damaged sites is low ($DS = 5 \times 10^{-10}$ ng min^{-1}), and TGF-β secretion rate from macrophages is high ($MS = 5 \times 10^{-9}$ ng min^{-1}); case DA: longer activation duration for latent TGF-β sources from damage sites by reducing secreting agents death rate by 100-fold ($AT = 1 \times 10^{-5}$ min^{-1}) in case D; case MA: longer activation duration of M2 macrophages by setting apoptosis rate of M2 macrophages to 0 in case M.

Longer activation of latent TGF-β sources caused localized fibrotic pattern

Next, we predicted the fibrotic outcomes with a longer activation duration of stationary or mobile sources. Latent TGF-β from damaged sites may remain activated for longer duration for severe lung tissue damage. The effects of the longer activation duration of stationary sources are shown in Fig 5A–5D. In this case, we turned off the secretion from mobile sources ($MS = 0$) to observe the response from damaged sites alone (case

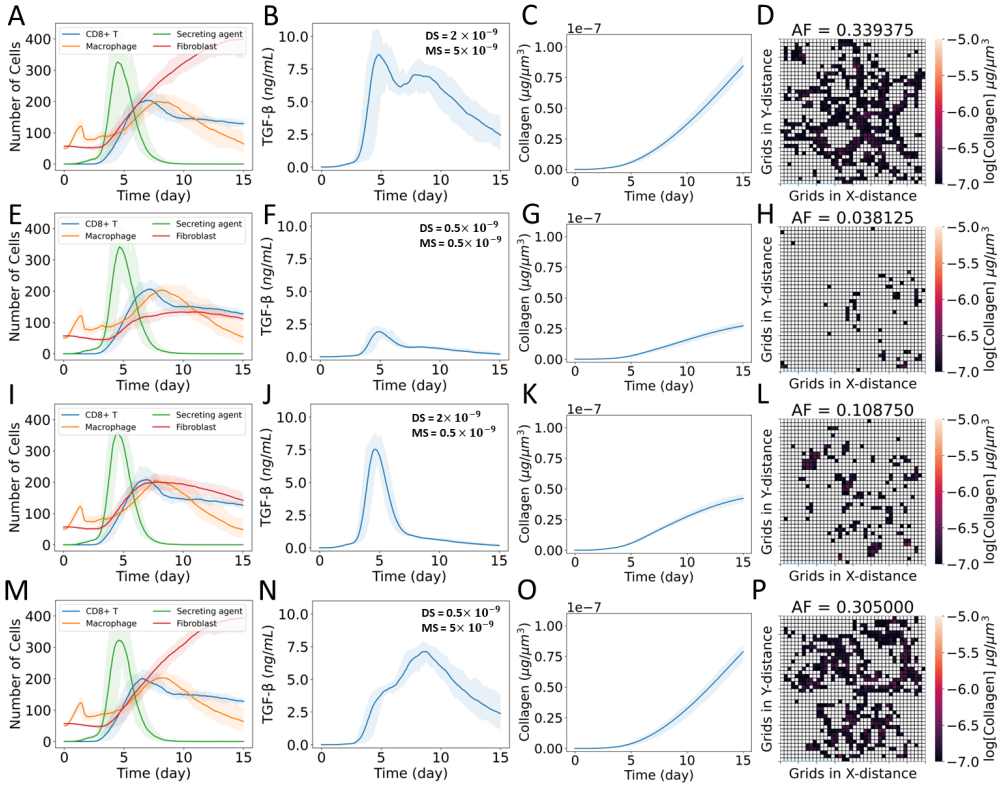

Fig 4. Effects of TGF-β production rates from damaged sites and macrophages. TGF-β production rate from (A–D) case DHMH: damaged sites is high ($DS = 2 \times 10^{-9}$ ng min^{-1}) and macrophages is high ($MS = 5 \times 10^{-9}$ ng min^{-1}); (E–H) case DLML: damaged sites is low ($DS = 5 \times 10^{-10}$ ng min^{-1}) and macrophages is low ($MS = 5 \times 10^{-10}$ ng min^{-1}); (I–L) case DHML: damaged sites is high ($DS = 2 \times 10^{-9}$ ng min^{-1}) and macrophages is low ($MS = 5 \times 10^{-10}$ ng min^{-1}); (M-P) case DLMH: damaged sites is low ($DS = 5 \times 10^{-10}$ ng min^{-1}) and macrophages is high ($MS = 5 \times 10^{-9}$ ng min^{-1}). Dynamics of (A, E, I, M) populations of CD8+ T cells, macrophages, latent TGF-β activation sites (secreting agents), and fibroblasts; (B, F, J, N) TGF-β concentration spatially averaged over the domain; (C, G, K, O) collagen concentration spatially averaged over the domain; (D, H, L, P) heat map showing collagen area fraction (AF) above threshold value of 1×10^{-7} μg μm^{-3}. The solid curves represent the mean of predictions and shaded areas represent the predictions between the 5th and 95th percentile of 15 replications of the agent-based model.

DA). We decreased the secreting agent death rate (AT) by 100-fold to extend the activation duration. Fig 5A showed larger accumulations of secreting agents over time, representing a longer activation duration of latent TGF-β. We observed higher concentrations of TGF-β with a peak value at an earlier phase of infection (Fig 5B). The spatial profile showed localized collagen fields with high concentrations of deposited collagen (Fig 5D). However, the violin plot of the collagen area fraction in Fig 3 showed results higher than case D and intermediate collagen area fraction compared to other cases. Therefore, even with a lower collagen fraction, localized damage with high collagen deposition can lead to long-term fibrosis by the dysregulation in the activation duration of latent TGF-β.

We observed localization of fibroblasts around 2 dpi with slow creation of stationary

sources (Fig S12), which disrupts around 5 dpi by the rapid creation of new stationary sources. The longer activation duration of stationary sources resulted in persistent localization of fibroblasts at the damaged sites from 5 dpi to 15 dpi. The localization pattern remains the same during that period due to a slow decrease of stationary sources. We also observed increases in accumulated fibroblasts in localized positions. In addition, we changed the initial placement of virions from uniform random distribution to Gaussian distribution at the tissue center for case DA; Fig S13 and S14 showed higher fibroblasts accumulation and dense collagen deposition near the center. So, fibrotic patterns vary depending on the location of initial infection sites.

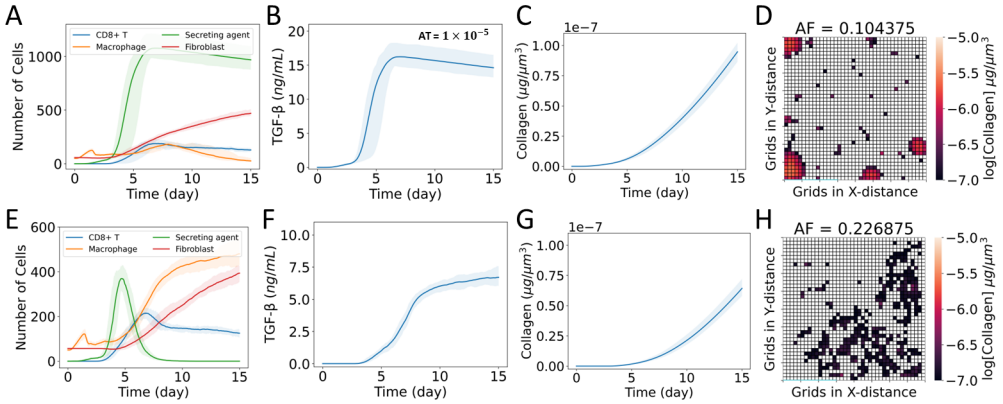

Fig 5. Effects of longer activation duration of stationary and mobile sources of TGF-β. Activation duration depends on secreting agent's death rate (AT). (A–D) Case DA: longer activation duration of latent TGF-β sources by reducing secreting agents death rate by 100-fold ($AT = 1 \times 10^{-5}$ min^{-1}) and secretion from macrophages are turned off ($MS = 0$ ng min^{-1}), (E–H) case MA: longer activation duration of M2 macrophages by setting apoptosis rate of M2 macrophages to 0 and activation from damaged sites are turned off ($DS = 0$ ng min^{-1}). Dynamics of (A, E) populations of CD8+ T cells, macrophages, latent TGF-β activation sites (secreting agents), and fibroblasts; (B, F) TGF-β concentration spatially averaged over the domain; (C, G) collagen concentration spatially averaged over the domain; (D, H) heat map showing collagen area fraction (AF) above threshold value of 1×10^{-7} μg μm^{-3}. The solid curves represent the mean of predictions and shaded areas represent the predictions between the 5th and 95th percentile of 15 replications of the agent-based model.

Sefik et al. [56] reported experimental results showing that severe SARS-CoV-2 infection increases human lung macrophage numbers at 4 dpi with a peak value at 14 dpi, and the number of macrophages remains high until 28 dpi. They also observed similar dynamics for the number of macrophages marked by CD206^{hi}, CD86^{+}, and CD169^{+} expression. CD206 is one of the major markers for M2 macrophages [57]. Sefik et al. [56] further reported persistent lung tissue pathology in the exudative, organizing, and fibrotic phases, with changed in effected tissue areas between 45% and 55% from uninfected tissue. We considered a similar scenario by setting the apoptosis rate of M2 macrophages to 0 and turning off the activation rate of latent TGF-β from damaged sites ($DS = 0$ ng min^{-1}) (case MA). In Fig 5E-5H, we showed the effects of longer activation of M2 macrophages. We observed a higher number of M2 macrophages in case MA compared to other cases (Fig 5E and S16). The simulated dynamics of M2 macrophages in case MA were also similar to experimental observations of Sefik et al. [56]. In Fig 5F, the spatially averaged TGF-β concentration increased over time, remained high, and shifted its peak value compared to case DA. We also observed a

higher collagen area fraction in case MA than in cases M and DA (Fig 3). The persistent presence of M2 macrophages caused a higher amount of collagen deposition, higher collagen area fraction, and localization of fibroblasts from 9 dpi to 15 dpi (Fig S15).

Partial removal of TGF-β changes fibrotic pattern

Finally, we considered the uptake of TGF-β by fibroblasts. We added an uptake term in Eq 3 to account for the change in concentration of TGF-β due to uptake by fibroblasts:

$$\frac{\partial T_\beta}{\partial t} = D_{T\beta}\nabla^2 T_\beta - \mu_{T\beta} T_\beta + \sum_{cells\ i} \delta(x - x_i)(E_{T\beta,i} - U_{F,i} F_{V,i} T_\beta) \tag{6}$$

where $U_{F,i}$ is the uptake rate of TGF-β by fibroblasts, and $F_{V,i}$ is the volume of fibroblasts. The uptake rate of TGF-β by fibroblasts was estimated based on model response (Table 2) and was assumed equivalent to the uptake rate of debris in the overall model.

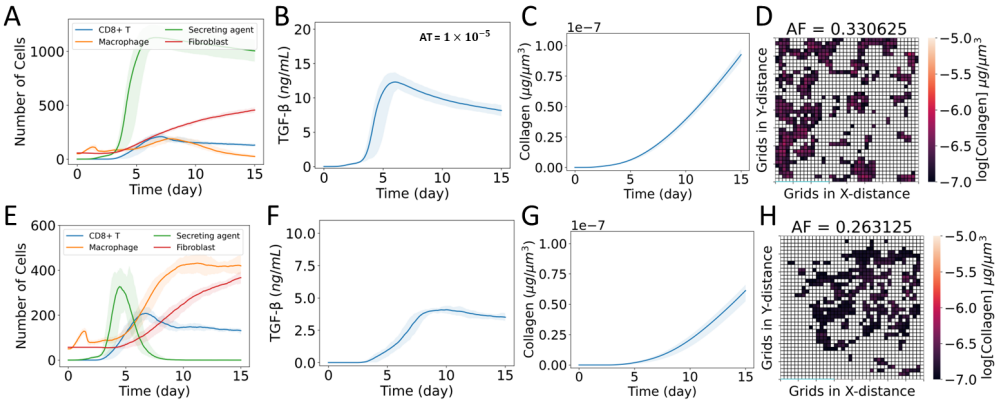

Fig 6. Effects of the uptake of TGF-β by fibroblasts. (A–D) Case DAU: uptake of TGF-β by fibroblasts in case DA, (E–H) case MAU: uptake of TGF-β by fibroblasts in case MA. Dynamics of (A, E) populations of CD8+ T cells, macrophages, latent TGF-β activation sites (secreting agents), and fibroblasts; (B, F) TGF-β concentration spatially averaged over the domain; (C, G) collagen concentration spatially averaged over the domain; (D, H) heat map showing collagen area fraction (AF) above threshold value of 1×10^{-7} μg μm^{-3}. The solid curves represent the mean of predictions and shaded areas represent the predictions between the 5th and 95th percentile of 15 replications of the agent-based model.

We considered the uptake of TGF-β in case DA and termed the new scenario as case DAU. Although the population dynamics and mean collagen concentrations remained similar, we observed variations in the mean TGF-β dynamics with a reduced peak value (Fig 6A - 6C). The uptake of TGF-β also changed the concentration gradient of TGF-β in the ECM, which caused delocalization and redistribution of fibroblasts in other tissue areas (Fig S17). As a result, we observed a significantly higher collagen area fraction in case DAU compared to cases D and DA (Fig 6D and S18). We also considered uptake of TGF-β in case MA and termed that scenario case MAU. Here, we observed change and reduction in spatially averaged TGF-β dynamics with similar population and spatially averaged collagen dynamics as case MA. Although the delocalization and redistribution of fibroblasts were observed in case MAU (Fig S19), collagen area fractions remained similar to case MA (Fig S18). We also observed higher collagen area fractions in case

DAU compared to case MAU. Our findings suggest that removing TGF-β from ECM when persistent latent TGF-β activation sites are present can spread fibrotic areas in tissue.

Our results give critical insight into the current clinical trials targeting TGF-β for lung fibrosis. At present, two of the promising anti-TGF-β drugs for lung fibrosis are pirfenidone and PLN-74809, and both are in Phase II clinical trials [58]. The mechanism of pirfenidone involves inhibiting the activity of TGF-β by stopping the maturation of latent TGF-β [59, 60]. The drug PLN-74809 inhibits $\alpha_V\beta_6$ and $\alpha_V\beta_1$ integrins to prevent the activation of latent TGF-β [61]. Since we observed changes in fibrotic pattern with changes in TGF-β sources and increases in collagen area fractions with the removal of TGF-β from ECM in the presence of persistent activation sites, the inclusion of spatial behavior, activation rate, and activation duration of sources is essential for a better outcome in current clinical trials. Partial removal of TGF-β from ECM or inhibition of TGF-β production from sources may change the chemotactic direction of fibroblasts and lead to fibrotic areas with higher collagen area fraction. It is essential to consider the spatial behavior and activity of sources before targeting them for inhibition of TGF-β as fibrosis is a spatial phenomenon.

Conclusions

The multiscale tissue simulator (overall model and fibrosis model) described here gives insight into the mechanisms and activity of TGF-β sources in fibroblast-mediated collagen deposition at damaged sites of SARS-CoV-2 infected tissue. We applied this model to investigate the spatial behaviors of sources of TGF-β, the production rate of TGF-β, and the activation duration of TGF-β sources in the process of lung fibrosis. Fibrosis is a spatial event; thus, it is essential to consider the spatial properties of the sources of the key biomarkers observed during the process. Our results showed localized collagen deposition from stationary sources of TGF-β and dispersed collagen deposition from mobile sources of TGF-β. Our results indicated that M2 macrophages and their persistent presence were mainly responsible for higher collagen area fractions. We predicted a longer activation of latent TGF-β sources could lead to fibrosis even with a lower collagen area fraction. Also, partial removal of TGF-β from ECM changed the chemotactic gradient of fibroblasts, resulting in a higher collagen area fraction. In the future, the accuracy of the predictions could further be improved by considering premorbidity of patient groups (e.g., hypertension), different phenotypes of fibroblasts (e.g., myofibroblasts), negative regulators for collagen degradation (e.g., MMP9), and collagen feedback to epithelial cells for regrowth and wound healing. The quantification of the collagen deposition dynamics depending on the activity of sources will benefit treatment strategies controlling TGF-β and help characterize the evolution of fibrosis in COVID-19 survivors.

Supporting information

Supplementary File The Supplementary File contains supporting information and figures organized into the following sections: TGF-β-dependent functions of fibroblasts (Fig S1); effects of TGF-β production rate from each source (Fig S2); fibroblast collagen production rate k_{FC}; dynamics of virions, neutrophils, DCs, and CD4 cells (Fig S3); effects of sources of TGF-β (Fig S4–S7); effects of production rate of TGF-β from combinations of sources (Fig S8–S11); effects of activation duration of sources (Fig S12–S16); and effects of uptake of TGF-β (Fig S17–S19).

Acknowledgments

This work was supported by the National Institutes of Health grant R35GM133763 (to A.N.F.V.), the University at Buffalo, and the Center for Computational Research at the University at Buffalo. We thank the scientific community for fibrosis model feedback, particularly Amber M. Smith, Thomas Hillen, and Yafei Wang.

References

1. Michalski JE, Kurche JS, Schwartz DA. From ARDS to pulmonary fibrosis: the next phase of the COVID-19 pandemic? Translational Research. 2022;241:13–24.
2. Li X, Shen C, Wang L, Majumder S, Zhang D, Deen MJ, et al. Pulmonary fibrosis and its related factors in discharged patients with new corona virus pneumonia: a cohort study. Respiratory Research. 2021;22(1):1–11.
3. Rai DK, Sharma P, Kumar R. Post covid 19 pulmonary fibrosis. Is it real threat? Indian Journal of Tuberculosis. 2021;68(3):330–333.
4. Meduri GU, Eltorky MA. Understanding ARDS-associated fibroproliferation. Intensive Care Medicine. 2015;41(3):517–520.
5. Jacobs JJ. Persistent SARS-2 infections contribute to long COVID-19. Medical Hypotheses. 2021;149:110538.
6. Tonelli R, Marchioni A, Tabbì L, Fantini R, Busani S, Castaniere I, et al. Spontaneous breathing and evolving phenotypes of lung damage in patients with COVID-19: review of current evidence and forecast of a new scenario. Journal of Clinical Medicine. 2021;10(5):975.
7. Nalbandian A, Sehgal K, Gupta A, Madhavan MV, McGroder C, Stevens JS, et al. Post-acute COVID-19 syndrome. Nature Medicine. 2021;27(4):601–615.
8. Ryan FJ, Hope CM, Masavuli MG, Lynn MA, Mekonnen ZA, Yeow AEL, et al. Long-term perturbation of the peripheral immune system months after SARS-CoV-2 infection. BMC Medicine. 2022;20(1):1–23.
9. John AE, Joseph C, Jenkins G, Tatler AL. COVID-19 and pulmonary fibrosis: A potential role for lung epithelial cells and fibroblasts. Immunological Reviews. 2021;302(1):228–240.
10. Yim J, Lim HH, Kwon Y. COVID-19 and pulmonary fibrosis: therapeutics in clinical trials, repurposing, and potential development. Archives of Pharmacal Research. 2021;44(5):499–513.
11. Zou JN, Sun L, Wang BR, Zou Y, Xu S, Ding YJ, et al. The characteristics and evolution of pulmonary fibrosis in COVID-19 patients as assessed by AI-assisted chest HRCT. PloS One. 2021;16(3):e0248957.
12. Han X, Fan Y, Alwalid O, Li N, Jia X, Yuan M, et al. Six-month follow-up chest CT findings after severe COVID-19 pneumonia. Radiology. 2021;299(1):E177–E186.
13. Matthay MA, Zemans RL, Zimmerman GA, Arabi YM, Beitler JR, Mercat A, et al. Acute respiratory distress syndrome. Nature Reviews Disease Primers. 2019;5(1):1–22.

14. Huang X, Xiu H, Zhang S, Zhang G. The role of macrophages in the pathogenesis of ALI/ARDS. Mediators of Inflammation. 2018;2018.

15. Bösmüller H, Matter M, Fend F, Tzankov A. The pulmonary pathology of COVID-19. Virchows Archiv. 2021;478(1):137–150.

16. Wendisch D, Dietrich O, Mari T, von Stillfried S, Ibarra IL, Mittermaier M, et al. SARS-CoV-2 infection triggers profibrotic macrophage responses and lung fibrosis. Cell. 2021;184(26):6243–6261.

17. Sheppard D. Transforming growth factor β: a central modulator of pulmonary and airway inflammation and fibrosis. Proceedings of the American Thoracic Society. 2006;3(5):413–417.

18. Sakai N, Tager AM. Fibrosis of two: Epithelial cell-fibroblast interactions in pulmonary fibrosis. Biochimica et Biophysica Acta (BBA)-Molecular Basis of Disease. 2013;1832(7):911–921.

19. Saito A, Horie M, Nagase T. TGF-β signaling in lung health and disease. International Journal of Molecular Sciences. 2018;19(8):2460.

20. Yue X, Shan B, A Lasky J. TGF-β: titan of lung fibrogenesis. Current Enzyme Inhibition. 2010;6(2):67–77.

21. Bonniaud P, Margetts PJ, Kolb M, Schroeder JA, Kapoun AM, Damm D, et al. Progressive transforming growth factor β1–induced lung fibrosis is blocked by an orally active ALK5 kinase inhibitor. American Journal of Respiratory and Critical Care Medicine. 2005;171(8):889–898.

22. Ferreira-Gomes M, Kruglov A, Durek P, Heinrich F, Tizian C, Heinz GA, et al. SARS-CoV-2 in severe COVID-19 induces a TGF-β-dominated chronic immune response that does not target itself. Nature Communications. 2021;12(1):1–14.

23. Vaz de Paula CB, Nagashima S, Liberalesso V, Collete M, da Silva FPG, Oricil AGG, et al. COVID-19: immunohistochemical analysis of TGF-β signaling pathways in pulmonary fibrosis. International Journal of Molecular Sciences. 2021;23(1):168.

24. Barron L, Gharib SA, Duffield JS. Lung pericytes and resident fibroblasts: busy multitaskers. The American Journal of Pathology. 2016;186(10):2519–2531.

25. Vaz de Paula CB, Nagashima S, Liberalesso V, Collete M, da Silva FPG, Oricil AGG, et al. COVID-19: Immunohistochemical Analysis of TGF-β Signaling Pathways in Pulmonary Fibrosis. International Journal of Molecular Sciences. 2022;23(1):168.

26. DeLeon-Pennell KY, Barker TH, Lindsey ML. Fibroblasts: the arbiters of extracellular matrix remodeling. Matrix Biology. 2020;91:1–7.

27. Good RB, Eley JD, Gower E, Butt G, Blanchard AD, Fisher AJ, et al. A high content, phenotypic 'scar-in-a-jar' assay for rapid quantification of collagen fibrillogenesis using disease-derived pulmonary fibroblasts. BMC Biomedical Engineering. 2019;1(1):1–10.

28. Ball L, Barisione E, Mastracci L, Campora M, Costa D, Robba C, et al. Extension of Collagen Deposition in COVID-19 Post Mortem Lung Samples and Computed Tomography Analysis Findings. International Journal of Molecular Sciences. 2021;22(14):7498.

29. B Moore B, Lawson WE, Oury TD, Sisson TH, Raghavendran K, Hogaboam CM. Animal models of fibrotic lung disease. American Journal of Respiratory Cell and Molecular Biology. 2013;49(2):167–179.

30. Li Xh, Fang Zn, Guan Tm, Lin Jj, Sun Ch, Huang Sy, et al. A novel collagen area fraction index to quantitatively assess bowel fibrosis in patients with Crohn's disease. BMC gastroenterology. 2019;19(1):1–7.

31. Brown BN, Price IM, Toapanta FR, DeAlmeida DR, Wiley CA, Ross TM, et al. An agent-based model of inflammation and fibrosis following particulate exposure in the lung. Mathematical Biosciences. 2011;231(2):186–196.

32. Warsinske HC, Wheaton AK, Kim KK, Linderman JJ, Moore BB, Kirschner DE. Computational modeling predicts simultaneous targeting of fibroblasts and epithelial cells is necessary for treatment of pulmonary fibrosis. Frontiers in Pharmacology. 2016;7:183.

33. Cogno N, Bauer R, Durante M. A 3D Agent-Based Model of Lung Fibrosis. Symmetry. 2022;14(1):90.

34. Ceresa M, Olivares AL, Noailly J, González Ballester MA. Coupled immunological and biomechanical model of emphysema progression. Frontiers in Physiology. 2018;9:388.

35. Hao W, Marsh C, Friedman A. A mathematical model of idiopathic pulmonary fibrosis. PLoS One. 2015;10(9):e0135097.

36. Jin YF, Han HC, Berger J, Dai Q, Lindsey ML. Combining experimental and mathematical modeling to reveal mechanisms of macrophage-dependent left ventricular remodeling. BMC Systems Biology. 2011;5(1):1–14.

37. Chowkwale M, Lindsey ML, Saucerman JJ. Intercellular model predicts mechanisms of inflammation-fibrosis coupling after myocardial infarction. The Journal of Physiology. 2022;.

38. Rikard SM, Athey TL, Nelson AR, Christiansen SL, Lee JJ, Holmes JW, et al. Multiscale coupling of an agent-based model of tissue fibrosis and a logic-based model of intracellular signaling. Frontiers in Physiology. 2019; p. 1481.

39. Getz M, Wang Y, An G, Becker A, Cockrell C, Collier N, et al. Iterative community-driven development of a SARS-CoV-2 tissue simulator. BioRxiv preprint. 2021;DOI: 10.1101/2020.04.02.019075.

40. Ghaffarizadeh A, Heiland R, Friedman SH, Mumenthaler SM, Macklin P. PhysiCell: An open source physics-based cell simulator for 3-D multicellular systems. PLoS Computational Biology. 2018;14(2):e1005991.

41. Pienaar E, Cilfone NA, Lin PL, Dartois V, Mattila JT, Butler JR, et al. A computational tool integrating host immunity with antibiotic dynamics to study tuberculosis treatment. Journal of theoretical biology. 2015;367:166–179.

42. Jenner AL, Aogo RA, Alfonso S, Crowe V, Deng X, Smith AP, et al. COVID-19 virtual patient cohort suggests immune mechanisms driving disease outcomes. PLoS Pathogens. 2021;17(7):e1009753.

43. Heiland R, Macklin P. pc4covid19; 2022.

44. Islam MA, Ford Versypt AN. covid19fibrosis; 2022.

45. Ghaffarizadeh A, Friedman SH, Macklin P. BioFVM: an efficient, parallelized diffusive transport solver for 3-D biological simulations. Bioinformatics. 2016;32(8):1256–1258.

46. SourceForge. Plot Digitizer. (Online; accessed 21-October-2021), `http://plotdigitizersourceforgenet/`. 2015;.

47. Yang F, Liu YH, Yang XP, Xu J, Kapke A, Carretero OA. Myocardial infarction and cardiac remodelling in mice. Experimental Physiology. 2002;87(5):547–555.

48. Trepat X, Chen Z, Jacobson K. Cell migration. Comprehensive Physiology. 2012;2(4):2369.

49. Padovan-Merhar O, Nair GP, Biaesch AG, Mayer A, Scarfone S, Foley SW, et al. Single mammalian cells compensate for differences in cellular volume and DNA copy number through independent global transcriptional mechanisms. Molecular Cell. 2015;58(2):339–352.

50. Lamond AI, Sleeman JE. Nuclear substructure and dynamics. Current Biology. 2003;13(21):R825–R828.

51. Roberts AB, Sporn MB, Assoian RK, Smith JM, Roche NS, Wakefield LM, et al. Transforming growth factor type beta: rapid induction of fibrosis and angiogenesis in vivo and stimulation of collagen formation in vitro. Proceedings of the National Academy of Sciences. 1986;83(12):4167–4171.

52. Ignotz RA, Massague J. Transforming growth factor-beta stimulates the expression of fibronectin and collagen and their incorporation into the extracellular matrix. Journal of Biological Chemistry. 1986;261(9):4337–4345.

53. Wahl SM, Hunt DA, Wakefield LM, McCartney-Francis N, Wahl LM, Roberts AB, et al. Transforming growth factor type beta induces monocyte chemotaxis and growth factor production. Proceedings of the National Academy of Sciences. 1987;84(16):5788–5792.

54. McDonough JE, Ahangari F, Li Q, Jain S, Verleden SE, Herazo-Maya J, et al. Transcriptional regulatory model of fibrosis progression in the human lung. JCI Insight. 2019;4(22).

55. Delorey TM, Ziegler CG, Heimberg G, Normand R, Yang Y, Segerstolpe Å, et al. COVID-19 tissue atlases reveal SARS-CoV-2 pathology and cellular targets. Nature. 2021;595(7865):107–113.

56. Sefik E, Israelow B, Mirza H, Zhao J, Qu R, Kaffe E, et al. A humanized mouse model of chronic COVID-19. Nature Biotechnology. 2022;40(6):906–920.

57. Tedesco S, Bolego C, Toniolo A, Nassi A, Fadini GP, Locati M, et al. Phenotypic activation and pharmacological outcomes of spontaneously differentiated human monocyte-derived macrophages. Immunobiology. 2015;220(5):545–554.

58. Shi N, Wang Z, Zhu H, Liu W, Zhao M, Jiang X, et al. Research progress on drugs targeting the TGF-β signaling pathway in fibrotic diseases. Immunologic Research. 2022; p. 1–13.

59. Hamidi SH, Kadamboor Veethil S, Hamidi SH. Role of pirfenidone in TGF-β pathways and other inflammatory pathways in acute respiratory syndrome coronavirus 2 (SARS-CoV-2) infection: a theoretical perspective. Pharmacological Reports. 2021;73(3):712–727.

60. Sathiyamoorthy G, Sehgal S, Ashton RW. Pirfenidone and nintedanib for treatment of idiopathic pulmonary fibrosis. Southern Medical Journal. 2017;110(6):393–398.

61. Cosgrove G, Decaris M, Wong S, Park E, Turner S, Adegbite E, et al. PLN-74809, an oral, dual-selective αvβ6/αvβ1 inhibitor in Phase 2 clinical trials for idiopathic pulmonary fibrosis (IPF), sustainably reduces transforming growth factor beta (TGF-β) activity in the lungs of healthy participants with once-daily dosing. In: D30. The Injured Lung: Mechanisms and Therapeutic Targets. American Thoracic Society; 2022. p. A5251–A5251.